Chaos, Solitons and Fractals 212 (2026) 119132

Contents lists available at ScienceDirect

Chaos, Solitons and Fractals

journal homepage: www.elsevier.com/locate/chaos

Spatiotemporal dynamics of epidemics in one-dimensional networks with diffusion-mediated coupling

Vitor H.A. Fávaro [a,*], Ricardo L. Viana [a,b], João P.V. Ramalho [c], Jane Rosa [d]

[a] Universidade Federal do Paraná, Departamento de Física, Curitiba, 81531-980, Paraná, Brazil
[b] Universidade Federal do Paraná, CICTI, NCC, Curitiba, Paraná, Brazil
[c] Universidade Federal do Paraná, Departamento de Informática, Curitiba, 81531-980, Paraná, Brazil
[d] Instituto Federal do Paraná, Campus Paranaguá, Paranaguá, 83215-750, Paraná, Brazil

ARTICLE INFO

Keywords:
Epidemic modeling
Reaction–diffusion systems
Numerical simulations

ABSTRACT

We investigate how spatial coupling mediated by a diffusing substance, modeled through chemical coupling, affects epidemic propagation in a one-dimensional network. Using the susceptible–infected–removed (SIR) epidemic model, we analyze how the coupling intensity D and the interaction range γ influence the spatiotemporal spreading of the disease. The interactions between sites decay exponentially with distance, allowing a transition between predominantly local and long-range spreading regimes. Our results reveal the emergence of distinct propagation patterns associated with different coupling regimes. For weak coupling intensities, the epidemic front propagates gradually through the network, whereas strong coupling intensities produce a qualitatively different regime characterized by nonmonotonic advancement rates near the outbreak focus. We also show how the coupling parameters affect the average propagation velocity, the global infection peak, the extinction time, and the temporal variability of the epidemic. These findings demonstrate that the coupling structure plays a central role in shaping the spatial organization and temporal evolution of epidemic spread.

1. Introduction

The spread of infectious diseases is a phenomenon in which biological, environmental, and social processes interact across multiple temporal and spatial scales [1–7]. In many scenarios, epidemic outbreaks emerge locally but may rapidly spread to distant regions, driven by human mobility, geographic connectivity, and heterogeneous interaction patterns [6,8–14].

Transmission can occur through different mechanisms, including direct or indirect contact between individuals, as well as environmental exposure such as contaminated water or food [15–18]. Regardless of the specific pathway, the resulting dynamics often depend on a combination of biological processes and patterns of human interaction.

Several pathogens exhibit wide geographic distribution and recurrent epidemic outbreaks, particularly in regions where environmental and social conditions favor transmission [19,20]. Their spread is strongly influenced by environmental factors such as temperature and precipitation, as well as by structural aspects including urbanization, population density, and human mobility patterns [10,19–24]. These elements contribute to highly complex dynamics and reinforce the need for approaches capable of integrating different descriptive scales [3,25].

* Corresponding author.
E-mail address: vitor.favaro@ufpr.br (V.H.A. Fávaro).

https://doi.org/10.1016/j.chaos.2026.119132
Received 8 July 2026; Received in revised form 19 August 2026; Accepted 1 September 2026
Available online 11 September 2026
0960-0779/© 2026 The Authors. Published by Elsevier Ltd. This is an open access article under the CC BY license (http://creativecommons.org/licenses/by/4.0/).

In this context, mathematical models play a fundamental role in investigating the mechanisms governing the transmission and spread of infectious diseases [26]. Classical compartmental models, such as the SIR (susceptible–infected–removed) model, provide a simplified yet effective description of the temporal evolution of epidemics in well-mixed populations [3,16,27]. From this framework, several extensions have been proposed to incorporate additional mechanisms or structure.

Despite their broad applicability, many of these models describe epidemiological dynamics only in temporal terms. They explicitly neglect the spatial structure in which transmission occurs [28]. In practice, disease propagation is strongly conditioned by geography, population flows, and connectivity between regions, being influenced by transportation systems and heterogeneous social interaction patterns [11,12,29–31]. As a consequence, initially localized outbreaks may evolve into regional or global epidemics, a phenomenon that cannot be adequately captured by purely well-mixed models [7–9,32].

To overcome these limitations, network-based approaches have been widely used to incorporate spatial and mobility effects into epidemiological models [6,11,13,18,23,24,33–36]. From this perspective, different regions are represented as nodes of a network, while the connections between them encode interactions or flows of individuals [25,30]. This type of structure makes it possible to systematically investigate how connectivity, interaction range, and human mobility influence the spatiotemporal patterns of infectious disease spread [4,8,9,37].

Mobility and spatial interactions have been represented in several distinct ways across the literature. Explicit migration or commuting fluxes between patches, often formulated within the metapopulation framework [38], appear in structured epidemic models [12,13,39], gravity-model formulations of interregional coupling [40], and mobility-informed spreading models based on large-scale airline traffic data [8,9,14,37,41], along with more recent multi-patch and graph-based frameworks [42,43]. These approaches generally define explicit rules for the movement or exchange of individuals between subpopulations.

Other approaches embed compartmental dynamics on network topologies without an explicit spatial metric [25,29,30,44,45], or describe spread through reaction–diffusion processes and distance-dependent nonlocal kernels, tracing back to the classical contact and traveling-wave models [46,47] and later integro-differential and metapopulation reaction–diffusion formulations [48–50], including comparative studies contrasting patch, distance-kernel, and network transmission models [11,51,52], as well as recent extensions to higher-order and temporal network structures [53]. These formulations differ from explicit mobility models in that spatial transmission may be represented through local diffusion or nonlocal influence kernels rather than through individual-based transport between patches.

The present work adopts a chemical-coupling framework in which spatial interactions are mediated by an auxiliary diffusive field rather than prescribed through explicit migration or commuting links [54–57]. Originally developed in the context of coupled oscillator and chemical oscillation theory [58–62], chemical coupling leads, under the appropriate reduction, to a weighted nonlocal interaction in which the local dynamics are influenced by a distance-dependent average of states at other sites [63]. Nonlocally coupled systems of this type exhibit a rich phenomenology, including spatial correlations and collective dynamical states [60,61]. In the present model, the interaction weights follow from the reduction of the underlying diffusion process, yielding an exponentially decaying kernel rather than a connectivity structure prescribed independently of spatial distance.

In this work, we formulate and implement the standard SIR model on a one-dimensional lattice of N sites connected by chemical coupling. The local SIR dynamics are used as the basis for the coupled system, while the chemical coupling provides the nonlocal spatial interaction between sites. We focus on the emergent behavior of the coupled system and investigate how the coupling intensity D and interaction range γ affect the average advancement rate, global infection peak, epidemic extinction time, and temporal variability.

The paper is organized as follows. Section 2 introduces the epidemiological SIR model together with the chemical coupling framework, including the governing equations for the network of coupled sites and the numerical procedures adopted in this work. Section 3 presents and discusses the numerical results. The final section is devoted to the conclusions.

2. Spatially coupled epidemiological model

The spread of infectious diseases is strongly influenced by spatial organization, human mobility, and the connectivity among different regions [8,9]. In many epidemic scenarios, outbreaks emerge locally and subsequently propagate through interconnected populations, producing complex spatiotemporal spreading patterns [4,11]. Daily population flows, regional displacements, and transportation systems create mechanisms through which infected individuals may introduce the disease into new locations, significantly affecting the global evolution of epidemics [6,10].

A common strategy for incorporating spatial structure into compartmental epidemic models is to consider a collection of locally well-mixed populations coupled through migration, diffusion, commuting, or other forms of spatial interaction [30,34,36,62]. Within this broad class of spatially coupled models, different formulations differ in how the interaction between populations is defined. In migration- and commuting-based metapopulation models, the coupling explicitly represents the transport of individuals between patches [8,9,12,13,42], whereas diffusion- and nonlocal-interaction formulations describe the spatial redistribution or influence of epidemiological states without necessarily assigning trajectories to individual hosts [11,37,46–48]. The present formulation belongs to the latter class and uses chemical coupling to represent a nonlocal spatial interaction mediated by an auxiliary diffusive field [54,58].

From an epidemiological perspective, chemical coupling is more precisely understood as a nonlocal, mean-field coupling of the epidemiological state variables, mediated by an auxiliary field that diffuses through the spatial domain, rather than as an explicit representation of individuals moving between subpopulations. The present model should therefore be interpreted as a phenomenological representation of spatial interaction mediated by a rapidly relaxing diffusive field, rather than as a mechanistic

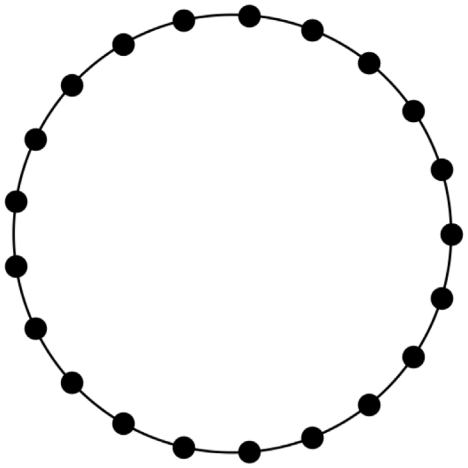


Fig. 1. Schematic representation of a regular first-neighbor network with periodic boundary conditions for $N = 21$.

model of individual mobility. In this formulation, the coupling does not track individual trajectories between sites; rather, it captures the collective effect of interregional interaction on local epidemic dynamics, allowing the epidemiological variables associated with different sites to influence one another. The introduction of an interaction range parameter further makes it possible to investigate different spatial spreading regimes, ranging from predominantly local interactions to effectively global coupling scenarios [54,55]. This interpretation relies on the mediating field relaxing fast enough for the adiabatic reduction to hold.

The local epidemiological dynamics at each site are described by the susceptible–infected–removed (SIR) model [15,27]. The population is divided into three epidemiological classes: susceptible, infected, and removed, denoted by $S(t)$, $I(t)$, and $R(t)$, respectively. The total population is assumed to remain constant over time, such that $S(t) + I(t) + R(t) = N_H$.

Susceptible individuals become infected through contact with infected individuals according to the infection rate β. Infected individuals recover at rate α and transition to the removed class. The local dynamics are therefore governed by the system of differential equations [15]

$$S'(t) = -\beta S I, \tag{1}$$

$$I'(t) = \beta S I - \alpha I, \tag{2}$$

$$R'(t) = \alpha I. \tag{3}$$

An initial number of infected individuals transmits the disease to susceptible individuals, causing the number of infected cases to grow until an epidemic peak is reached. Afterwards, the infected population decreases as individuals recover and enter the removed class. The epidemic potential is characterized by the basic reproduction number

$$R_0 = \frac{\beta S(0)}{\alpha}, \tag{4}$$

where $S(0)$ represents the initial number of susceptible individuals. This quantity measures the average number of secondary infections generated by a single infected individual introduced into a fully susceptible population [2]. If $R_0 > 1$, the disease can spread through the population and generate an epidemic outbreak. Conversely, if $R_0 \leq 1$, the infection cannot sustain transmission and eventually disappears [15].

To incorporate spatial effects, we consider a one-dimensional network composed of N equally spaced sites with periodic boundary conditions, so that the first and last sites also interact, as illustrated in Fig. 1. Each site represents a geographic region whose local dynamics are governed by the SIR model, while the interaction among regions occurs through chemical coupling. The ring topology adopted here is consistent with the periodic boundary conditions used in the underlying one-dimensional chemical-coupling formulation. Extending the exponential kernel to two-dimensional or heterogeneous topologies would require re-deriving the interaction kernel for those geometries, which lies outside the scope of the present work.

Formally, each site j is described by a state vector $\mathbf{X}_j(t) \in \mathbb{R}^M$, whose local dynamics are governed by a vector field $\mathbf{F}(\mathbf{X}_j)$. Chemical coupling is incorporated through an additional term proportional to a weighted average of neighboring sites [54]. Let $\mathcal{N} = (N-1)/2$ denote the number of neighbors considered on each side. The coupled system is then written as

$$\frac{d\mathbf{X}_j}{dt} = \mathbf{F}(\mathbf{X}_j) - \mathbf{C}\left[\mathbf{X}_j - B\sum_{\ell=1}^{\mathcal{N}} e^{-\gamma\ell\Delta}\left(\mathbf{X}_{j-\ell} + \mathbf{X}_{j+\ell}\right)\right]. \tag{5}$$

Here, ℓ denotes the discrete lattice distance, i.e., the number of sites separating node j from its neighbors, while Δ represents the physical spacing between consecutive lattice sites [54]. Moreover, $\mathbf{C}$ is a matrix specifying which components are subject to

coupling, and B is the normalization constant given by

$$B = \left[2 \sum_{\ell=1}^{\mathcal{N}} e^{-\gamma \ell \Delta} \right]^{-1}. \tag{6}$$

The exponential kernel used here is motivated by the chemical-coupling reduction of Kuramoto developed for one-dimensional oscillator lattices by Viana et al. [54]. In that framework, each site secretes an auxiliary field governed by a diffusion–degradation equation, whose stationary spatial profile decays exponentially with distance. This motivates the discrete kernel $e^{-\gamma \ell \Delta}$ adopted in the present formulation, where γ controls the characteristic coupling length. The normalization constant B is introduced so that the corresponding discrete weights sum to unity over the $\mathcal{N}$ neighbors considered on each side of a given site. In the present epidemiological model, this kernel is incorporated into a relaxational coupling term that drives each local state toward a weighted average of the states at other sites. Thus, the resulting interaction can be interpreted as a discrete nonlocal diffusive coupling, consistent with spatial coupling formulations used in reaction–diffusion epidemic models [46–50].

For simplicity, we adopt units in which the inter-site spacing is unity, i.e. $\Delta = 1$. With this choice the spatial factor simplifies to $e^{-\gamma \ell}$ and the summations above run over the discrete lattice distances $\ell = 1, \ldots, \mathcal{N}$.

Thus, the influence of one site on another decays exponentially with distance, controlled by the range parameter γ. Large values of γ emphasize local interactions ($\gamma \to \infty$), small values approach global coupling ($\gamma = 0$), and intermediate values ($0 < \gamma < \infty$) correspond to long-range coupling. In the present work, the local-interaction regime is represented by $\gamma = 15$.

Although this formulation was originally introduced for networks of coupled oscillators, here it is adapted to an epidemiological context, with each site representing a geographical unit and the chemical coupling capturing the collective, mean-field effect of spatial interaction on local epidemic dynamics, as discussed above. In this framework, spatial disease propagation emerges because the coupling allows the epidemiological state variables at one site to influence the local dynamics at other sites, with the strength of this influence decaying exponentially with distance.

Assuming that the local dynamics at each site are governed by the SIR model [Eqs. (1)–(3)], we define

$$\mathbf{X}_j = \begin{pmatrix} S_j \\ I_j \\ R_j \end{pmatrix}, \qquad \mathbf{F}(\mathbf{X}_j) = \begin{pmatrix} -\beta S_j I_j \\ \beta S_j I_j - \alpha I_j \\ \alpha I_j \end{pmatrix}.$$

We take $\mathbf{C} = \mathrm{diag}(D, D, D)$, where D represents the coupling intensity in day^{-1} and is applied identically to the three state variables. This choice is intended as a controlled baseline rather than as a realistic assumption about epidemiological mobility. Infected individuals may exhibit different mobility patterns from the general population, so allowing distinct effective coupling intensities for each compartment is a natural extension of the present model. Substitution into Eq. (5) yields

$$S_j'(t) = -\beta S_j I_j - D \left[S_j - B \sum_{\ell=1}^{\mathcal{N}} e^{-\gamma \ell} (S_{j-\ell} + S_{j+\ell}) \right], \tag{7}$$

$$I_j'(t) = \beta S_j I_j - \alpha I_j - D \left[I_j - B \sum_{\ell=1}^{\mathcal{N}} e^{-\gamma \ell} (I_{j-\ell} + I_{j+\ell}) \right], \tag{8}$$

$$R_j'(t) = \alpha I_j - D \left[R_j - B \sum_{\ell=1}^{\mathcal{N}} e^{-\gamma \ell} (R_{j-\ell} + R_{j+\ell}) \right], \tag{9}$$

which governs the spatiotemporal evolution of the epidemic along the network. The exponentially weighted summation accounts for interactions with distance-dependent decay, and the parameter D regulates the overall strength of the spatial coupling. Exponentially-decaying coupling kernels of this kind have already been considered in metapopulation and reaction–diffusion epidemic models [48,51]. In the present formulation, the coupling intensity D and the interaction range γ enter as independent parameters, allowing the strength and the spatial reach of the interaction to be varied separately.

To verify that the total population of the network is conserved, we sum the evolution equations over all classes and all sites. Defining the total population of site j as $N_j(t) = S_j(t) + I_j(t) + R_j(t)$, the local contribution from the SIR dynamics alone vanishes, since infection and recovery only move individuals between classes within the same site. Only the coupling term therefore contributes to the evolution of N_j, so that adding Eqs. (7)–(9) for a given site j gives

$$\frac{dN_j}{dt} = -D \left[N_j - B \sum_{\ell=1}^{\mathcal{N}} e^{-\gamma \ell} \left(N_{j-\ell} + N_{j+\ell} \right) \right]. \tag{10}$$

Summing this expression over all N sites and using the periodicity of the lattice, each shifted sum $\sum_j N_{j-\ell}$ and $\sum_j N_{j+\ell}$ reduces to $\sum_j N_j$, so that the bracketed term becomes $\sum_j N_j - B \cdot 2\left(\sum_\ell e^{-\gamma \ell}\right) \sum_j N_j$, which vanishes identically once the normalization $B = [2 \sum_{\ell=1}^{\mathcal{N}} e^{-\gamma \ell}]^{-1}$ is substituted. Therefore,

$$\frac{d}{dt} \sum_{j=1}^{N} N_j(t) = 0. \tag{11}$$

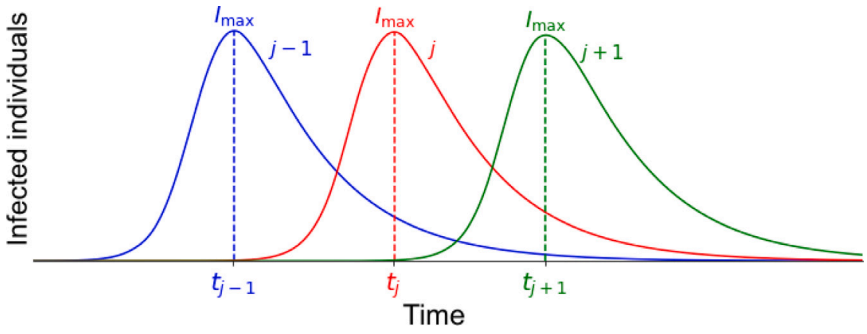


Fig. 2. Schematic representation of infection peaks at neighboring sites. The peak times t_{j-1}, t_j, and t_{j+1} are used to compute the time difference Δt in the definition of the advancement rate.

Thus, the total network population is conserved. Moreover, the coupling operator conserves the network-wide total of each epidemiological compartment separately, whereas the local SIR reactions transfer individuals from S to I and from I to R. This conservation property does not imply a mechanistic interpretation in terms of individual migration, commuting fluxes, or explicitly prescribed transport events between sites.

For the numerical implementation we developed a program in the C programming language to solve numerically the Eqs. (7)–(9) using the fourth-order Runge–Kutta method with a fixed time step $\Delta t = 0.01$. In the simulations of Eqs. (7)–(9) the parameter values were fixed to those reported in Ref. [15]: $\beta = 0.002342$ ind.$^{-1}$day^{-1} and $\alpha = 0.476$ day^{-1}.

The basic reproduction number for the parameter set used in the simulations is $R_0 = 4.92$, computed using $N_H = 1000$ individuals per site and the parameter values listed above. All simulations were performed for a total of $N = 1001$ coupled sites, each containing 1000 susceptible individuals, except for site $j = 501$, where a single infected human individual was introduced.

The resolution of the parameter grid was adjusted according to the type of analysis performed. For the two-parameter analyses, in which D and γ were varied simultaneously, 110 values of D were sampled over $10^{-5} \leq D \leq 1.0$ and 1500 values of γ over $0.0 \leq \gamma \leq 15.0$. When the analysis focused specifically on the dependence on D, a finer grid of 1000 values of D was used over the same range.

To quantify how the disease spreads as a function of the structural parameters D and γ, we employ the following observables: the average advancement rate v_m, the extinction time τ, the global infection peak $\mathcal{I}^{(\text{peak})}$, and the coefficient of variation CV. Definitions and computational details for these quantities are given below.

The advancement rate quantifies the speed at which infection propagates through the network. For this purpose, we consider the time at which each site reaches its peak number of infected individuals ($I_{\max}$) and compare these times between different sites. We define the advancement rate as $v = |\Delta x|/\Delta t$, where Δx is the distance between analyzed sites and Δt is the difference between the times at which each site reaches its infection peak.

Taking site $j = 501$ as the reference, we analyze neighboring sites located at a distance n from this position, such that $i = j \pm n$, with $n = 1, 2, \ldots, (N-1)/2$. The corresponding advancement rate is defined as

$$v_i = \frac{|i-j|}{t_i - t_j}. \tag{12}$$

For illustration, consider Fig. 2, which shows the peak times for neighboring sites. Each curve displays the infected population at a specific site, with dashed vertical lines marking the respective peak times t_{j-1}, t_j, and t_{j+1}. The intervals between these maxima define Δt, forming the basis for the calculation of the advancement rate.

A global characterization of the epidemic spread across the network is obtained by computing the average advancement rate,

$$v_m = \frac{1}{n_t} \sum_i v_i, \tag{13}$$

where n_t is the total number of sites considered in the calculation.

In addition to the advancement rate, which characterizes how fast the epidemic propagates across the network, we introduce a second temporal quantifier: the epidemic extinction time. While the advancement rate captures the speed of spatial spread, the extinction time measures how long the epidemic persists in the system.

We define the extinction time as the instant at which a fixed fraction of the total population has transitioned to the removed compartment. Let $R_{\text{tot}}(t) = \sum_{j=1}^{N} R_j(t)$ denote the total number of removed individuals in the network, where N_{tot} is the total population size. The extinction time τ is then defined as

$$\tau = \min \left\{ t : \frac{R_{\text{tot}}(t)}{N_{\text{tot}}} \geq 0.95 \right\}. \tag{14}$$

This threshold-based criterion reflects the moment when the epidemic has effectively exhausted the susceptible pool and the outbreak is no longer dynamically sustained. From a mathematical standpoint, extinction does not necessarily imply the complete

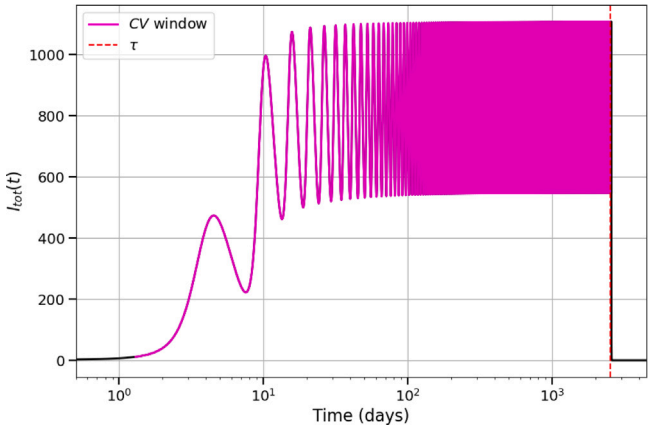


Fig. 3. Representative time series of the total number of infected individuals $I_{tot}(t)$. The magenta segment indicates the interval used to compute the coefficient of variation CV. The vertical dashed red line marks the extinction time τ, which sets the upper bound of the statistical window. (For interpretation of the references to color in this figure legend, the reader is referred to the web version of this article.)

disappearance of infected individuals, since residual infections may persist at very low levels. Instead, it marks the transition to a regime where large-scale transmission has ceased and the system approaches a stationary state.

As a complementary measure, we introduce the global infection peak, which quantifies the maximum instantaneous infectious burden in the network. Instead of focusing on individual sites, this quantity captures the collective epidemic intensity at the macroscopic scale.

For the model, we compute the total number of infected individuals at time t by summing over all sites

$$I_{tot}(t) = \sum_{j=1}^{N} I_j(t), \tag{15}$$

and define the global infection peak as the maximum of this quantity over time

$$I^{(\text{peak})} = \max_t I_{tot}(t). \tag{16}$$

To further characterize the dynamical behavior, we introduce the coefficient of variation CV, defined as

$$CV = \frac{\sigma}{\mu}, \tag{17}$$

where σ and μ are the standard deviation and mean of the infected time series (computed up to extinction). The CV is computed only over the active epidemic interval, from the beginning of the dynamics up to the extinction time τ, with a lower bound $t_{\min}$ defined as the first time at which the number of infected individuals reaches at least ten, so that the coefficient of variation is evaluated in the interval $t_{\min} \le t \le \tau$. A representative example of the temporal interval used in the calculation of the coefficient of variation is shown in Fig. 3.

Taken together, the advancement rate, extinction time, global infection peak, and coefficient of variation provide a structured characterization of the epidemic dynamics across spatial and temporal scales. Since all these quantities are evaluated as functions of the coupling intensity D and the coupling range γ, they allow us to assess how chemical coupling reshapes propagation speed, outbreak duration, epidemic severity, and temporal variability. This framework forms the basis for the analysis presented in the following section.

3. Results

This section first examines the local propagation of the epidemic front at selected sites, with emphasis on how the infection spreads away from the outbreak location. Next, we analyze the temporal evolution of the total number of infected individuals, which reveals how the global dynamics depend on the interaction range. Finally, we summarize the behavior of the coupled system using colormaps of the average advancement rate, the global infection peak, and the extinction time across the full parameter space.

The temporal evolution of the susceptible and infected populations at selected sites is shown in Fig. 4. The epidemic dynamics are initiated from the reference site $j = 501$, where a single infected individual is introduced into the system. Specifically, the initial conditions are set as $I(0) = 1$ and $S(0) = N_H - 1$ at the reference site $j = 501$, while for all other sites, the population starts at $I(0) = 0$ and $S(0) = N_H$. From this initial configuration, the infection propagates through the network due to the coupling among sites. The spreading process occurs in both spatial directions, namely toward the right ($j = 502, 503, \ldots$) and toward the left ($j = 500, 499, \ldots$) of the reference site. Nevertheless, in order to improve the visualization and avoid redundant information, only the sites located to the right of the reference site are displayed in Fig. 4.

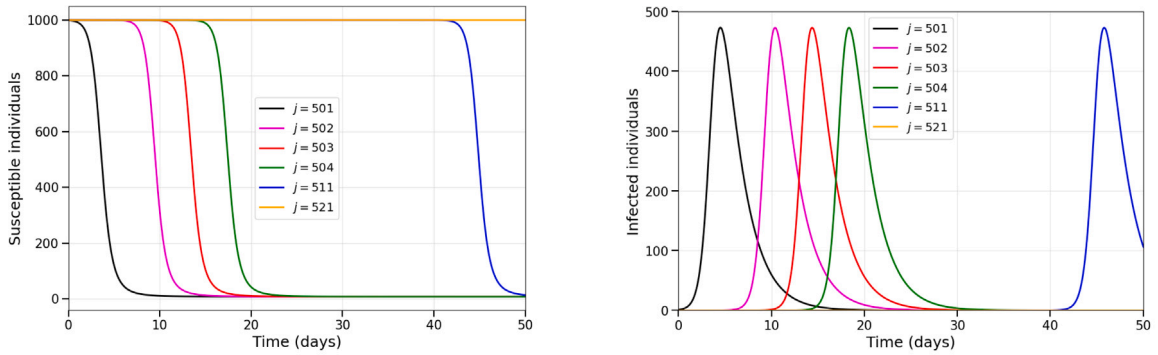


Fig. 4. Temporal evolution of the populations of (a) susceptible and (b) infected individuals at selected sites during the propagation of the epidemic front from the initial outbreak location $j = 501$. Results correspond to $\gamma = 7.5$ and coupling intensity $D = 10^{-5}$ day^{-1}.

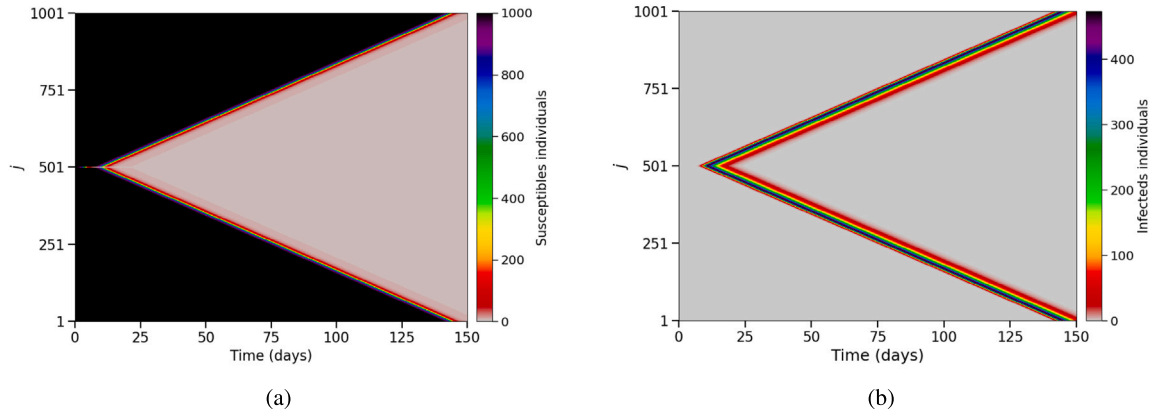


Fig. 5. Colormaps of the (a) susceptible and (b) infected individuals across the network, illustrating the collective traveling-wave propagation of the epidemic front. Results correspond to $\gamma = 0.5$ and coupling intensity $D = 10^{-5}$ day^{-1}. (For interpretation of the references to color in this figure legend, the reader is referred to the web version of this article.)

In Fig. 4(a), the susceptible population remains close to its initial value at sites far from the outbreak source during the early stages of the dynamics, since the infection has not yet propagated to these regions. As time evolves, however, the epidemic front progressively moves through the network, leading to a gradual depletion of susceptible individuals at each site through the coupling-induced infection process. This reduction does not occur simultaneously across the lattice; instead, each site experiences the epidemic at a different instant depending on its distance from the reference site ($j = 501$). Consequently, sites closer to the outbreak focus are affected earlier, whereas more distant regions respond only after a noticeable delay, revealing the finite propagation speed of the epidemic front.

The dynamics of the infected population, shown in Fig. 4(b), exhibit transient peaks that emerge at the outbreak focus ($j = 501$) and subsequently propagate through neighboring sites with similar temporal delays. Unlike the monotonic decrease observed for the susceptible population, the infected individuals first increase as the epidemic front reaches a given site and later decrease as recovery processes dominate the local dynamics. As the front advances through the network, the sequence of delayed infection peaks progressively shifts across the lattice, characterizing a traveling-wave-like propagation of the epidemic away from the initial outbreak region.

To provide a more complete description of the epidemic dynamics over the entire network, Fig. 5 presents colormaps of the susceptible S and infected I populations for the coupled SIR model. Unlike the analysis based on selected sites, these colormaps allow the simultaneous visualization of the temporal evolution of all regions of the network, highlighting the collective propagation of the epidemic through the network.

Fig. 5(a) shows the progressive depletion of susceptible individuals as the epidemic front advances through the system. Initially, most regions preserve values close to the initial condition, but as time evolves the susceptible population decreases sequentially across neighboring sites, producing a clear chain-like spreading process. The moving transition region separating affected and unaffected areas characterizes the propagation of the epidemic front with finite velocity.

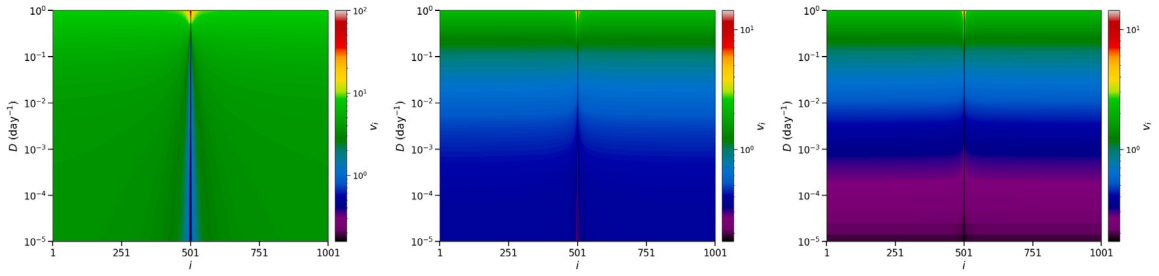


Fig. 6. Colormaps of the advancement rate υ_i as a function of the coupling intensity D (day^{-1}), for three representative values of the interaction range: (a) $\gamma = 0.5$, (b) $\gamma = 5.0$, and (c) $\gamma = 15.0$. (For interpretation of the references to color in this figure legend, the reader is referred to the web version of this article.)

The infected population, shown in Fig. 5(b), exhibits a localized propagating structure associated with the active epidemic region. As the front reaches a given site, the infected density increases due to the interaction between susceptible and infected individuals, and subsequently decreases as recovery processes dominate the dynamics. Consequently, regions behind the front contain fewer infected individuals, while regions ahead of it remain essentially disease free.

To investigate how the epidemic front propagates through the network, Fig. 6 presents colormaps of the advancement rate for each site (υ_i) for three representative values of the interaction range γ. It is important to emphasize that $\gamma \to 0$ approaches the global coupling limit, intermediate values represent long-range interactions, and the limit of local (nearest-neighbor) interactions ($\gamma \to \infty$) is effectively reached at $\gamma = 15$. These maps reveal how the coupling intensity D and the interaction range shape the spatial propagation of the epidemic front across the lattice.

For smaller values of γ, such as in Fig. 6(a), distant sites contribute more significantly to the spreading dynamics. In this regime, the epidemic front propagates rapidly across the network even for relatively small values of the coupling intensity D, indicating that the long-range contributions facilitate the spatial propagation of the infection through the network. As a consequence, the advancement rates remain comparatively large over a broad spatial region, and the propagation patterns become more spatially homogeneous.

As γ increases, the interactions become progressively more localized around neighboring sites. This behavior is clearly observed in Fig. 6(b) and becomes even more pronounced in Fig. 6(c). In these cases, epidemic propagation depends more strongly on spatial interactions between adjacent sites, producing smoother spatial variations in the advancement rates. Consequently, the propagation front advances more gradually through the network, especially for smaller values of the coupling intensity D.

The most prominent feature of Fig. 6, however, is the behavior of the advancement rates in the vicinity of the outbreak site ($j = 501$). Two qualitatively distinct propagation regimes can be identified. For relatively weak coupling, the advancement rate varies smoothly across the lattice, producing a nearly monotonic spatial profile. As the coupling intensity increases beyond a critical value D_{crit}, however, the propagation near the outbreak focus becomes locally accelerated, generating a region with significantly larger advancement rates than those observed at neighboring sites. Since the value of D_{crit} depends on the interaction range γ, the transition between these regimes occurs at different coupling intensities for each panel of Fig. 6.

To illustrate these propagation regimes more clearly, Fig. 7(a) presents representative velocity profiles for different values of the coupling intensity D with fixed interaction range $\gamma = 15$. By selecting specific values of the coupling intensity, the figure allows a direct comparison between the distinct spatial organizations of the advancement rates observed in the colormaps of Fig. 6.

As illustrated in Fig. 7(a), the advancement-rate profiles υ_i provide a clearer view of the transition identified in the colormaps of Fig. 6. For coupling intensities below a critical value D_{crit}, the advancement-rate profile remains approximately monotonic, with the velocity decreasing smoothly away from the outbreak site. In this regime, the epidemic front advances in a relatively homogeneous manner throughout the network.

Once the coupling exceeds D_{crit}, however, the propagation profile changes qualitatively. A pronounced peak develops at the outbreak focus ($j = 501$), indicating that the epidemic front becomes locally accelerated around the reference site while the advancement rates at more distant locations remain comparatively smaller. Consequently, the spatial profile becomes nonmonotonic, demonstrating that increasing the coupling intensity does not simply accelerate the epidemic front uniformly throughout the network. Instead, the enhancement of the propagation becomes concentrated around the outbreak focus, leading to a transition from an approximately homogeneous propagation regime to one characterized by localized acceleration near the epidemic source.

To quantify the onset of this transition, we define the critical coupling parameter D_{crit} as the smallest value of D for which the advancement rate at the outbreak site exceeds that of its nearest neighbors. The dependence of D_{crit} on the interaction range is shown in Fig. 7(b).

The dependence of D_{crit} on the interaction range, shown in Fig. 7(b), demonstrates that the onset of the accelerated propagation regime is not universal but is instead controlled by the spatial structure of the coupling. Consequently, the different color patterns observed in Fig. 6 correspond to the same transition occurring at different coupling intensities for each value of γ.

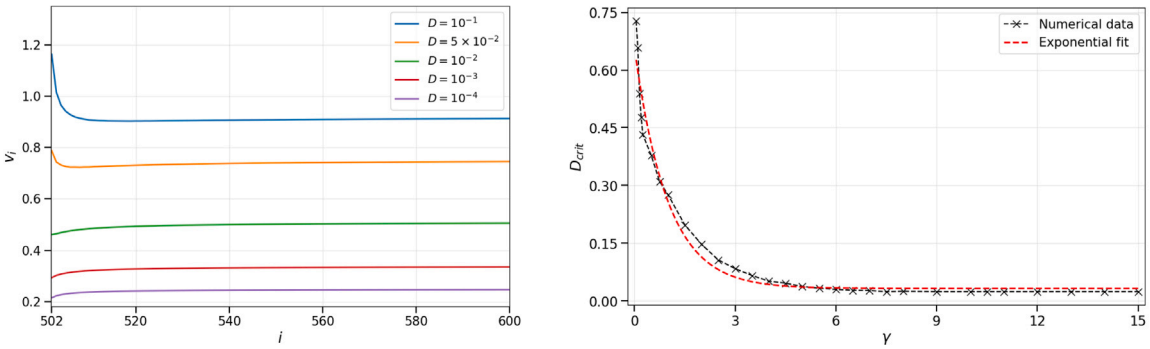


Fig. 7. (a) Advancement rates relative to the reference site $j = 501$ for different values of the coupling intensity D (day^{-1}), with $\gamma = 15$. (b) Critical coupling coefficient D_{crit} as a function of the interaction range parameter γ; the black curve with $\times$ markers represents the numerical values of D_{crit}, while the red dashed line shows an exponential crossover fit of the form $D_{crit}(\gamma) \sim ce^{-a\gamma} + D_{\text{plateau}}$. (For interpretation of the references to color in this figure legend, the reader is referred to the web version of this article.)

The monotonic decrease of D_{crit} with γ indicates that progressively weaker coupling is required to trigger the accelerated propagation regime as the interactions become more localized. For $\gamma = 0$, the coupling becomes global, yielding a mean-field-like spatial interaction, requiring relatively large coupling to generate the initial velocity overshoot at the focus. Increasing γ causes the interactions to become progressively more localized, first long-ranged and structured, and eventually reducing to nearest-neighbor coupling in the large-γ limit (which is reached in our model for $\gamma \geq 15$). In this regime, spatial heterogeneities play a more prominent role, and weaker coupling is sufficient to produce the same nonmonotonic response, leading to the observed saturation of D_{crit}.

As shown by the red dashed line in Fig. 7(b), the dependence of D_{crit} on γ is well described by an exponential crossover of the form $D_{crit}(\gamma) \sim ce^{-a\gamma} + D_{\text{plateau}}$, with a finite saturation value at large interaction ranges. The fit yields $c = 0.63 \pm 0.02$, $a = 1.02 \pm 0.10$, and $D_{\text{plateau}} = 0.032 \pm 0.008$. This behavior quantitatively characterizes the smooth crossover between propagation regimes controlled by the interaction range γ, which sets the characteristic spatial scale of the dynamics.

Therefore, the interaction range not only controls the overall propagation speed of the epidemic front but also determines the coupling threshold at which the transition from homogeneous to locally accelerated propagation occurs. These results demonstrate that the spatial organization of the interactions governs both the speed and the qualitative structure of epidemic spreading across the network.

The nonmonotonic regime is not an artifact of the peak-time-based velocity definition, as alternative definitions of the propagation speed based on absolute infection thresholds and local peak fractions yield consistent results for different values of the coupling intensity D. Since D acts identically on all compartments, the effect is also not associated with a distinct enhancement of infected mobility. Instead, the results are consistent with a coupling-induced spatial redistribution of the epidemic state, whereby neighboring sites reach substantially higher infection levels before the reference site reaches its peak, reducing the temporal separation between their epidemic peaks and producing the observed local increase in the measured propagation rate. From an epidemiological perspective, this behavior indicates that spatial coupling can compress the timing of local epidemic peaks. However, its broader significance depends on the specific coupling structure adopted and should be further investigated using models with more detailed compartment-specific coupling and transmission processes.

Having characterized the local propagation of the epidemic front and its spatial structure, we now turn to a global perspective. We analyze the total number of infected individuals $I_{tot}(t)$, which aggregates the dynamics over all sites and captures how the interaction range γ affects the overall temporal evolution of the outbreak. Fig. 8 shows this behavior for representative values of γ.

For large values of γ, as presented in Fig. 8(a), where interactions are predominantly short-range, the system initially undergoes a transient stage characterized by localized outbreaks with relatively small amplitudes. At later times, the infected population exhibits pronounced variations over time and the epidemic persists for thousands of days before eventually reaching extinction. This behavior is associated with the localized propagation of the epidemic, which allows the outbreak to develop successively across different regions of the network rather than activating the entire system within a short time interval.

For the intermediate interaction range illustrated in Fig. 8(b), the epidemic still develops over an extended time interval, but the longer interaction range promotes a more coordinated propagation across the network. As a consequence, the infected population remains at a substantially higher average level, while the temporal variations are less pronounced than those observed for $\gamma = 15$. Thus, increasing the interaction range of the coupling progressively enhances the spatial coordination of epidemic activity.

Conversely, for small values of γ, depicted in Fig. 8(c), the long-range coupling strongly reduces the temporal separation between the epidemic responses of different sites. A large fraction of the network is therefore activated within a relatively short time interval, resulting in a single broad epidemic event with an exceptionally high global infection peak ($I_{tot} > 15000$). As highlighted in the inset, the infected population remains close to a broad maximum over this interval. The rapid and spatially widespread transmission also

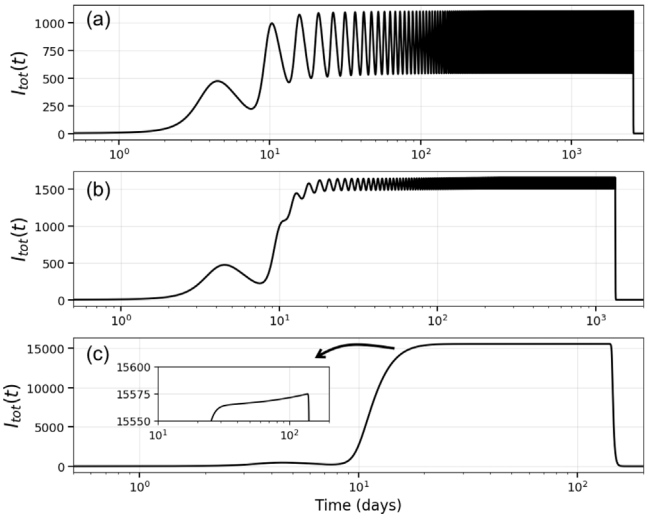


Fig. 8. Evolution of the number of infected individuals over time with coupling intensity $D = 10^{-5}$ day^{-1}. Panels correspond to (a) $\gamma = 15.0$, (b) $\gamma = 5.0$, and (c) $\gamma = 0.5$. The x-axis is presented on a logarithmic scale to highlight the long-term behavior. The inset in panel (c) provides a magnified view of the dynamics, highlighting the absence of fluctuations in this regime.

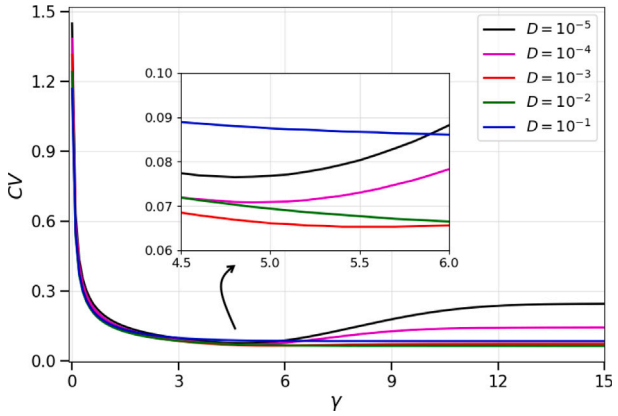


Fig. 9. Coefficient of variation (CV) of the total number of infected individuals as a function of the interaction range γ, for coupling intensities ranging from $D = 10^{-5}$ to $D = 10^{-1}$ day^{-1}. The CV is defined as the ratio between the standard deviation and the mean (σ/μ) of the time series up to the extinction time τ. The inset provides a magnified view of the region $4.5 \lesssim \gamma \lesssim 6$, where the local minimum around $\gamma \approx 5$ for lower coupling intensities is visible.

accelerates the depletion of susceptible individuals, leading to a substantially shorter epidemic lifetime than those observed for more localized interactions.

To complement the temporal analysis, we evaluate how the variability of the infected population changes with γ through the coefficient of variation CV, as shown in Fig. 9. The coefficient of variation measures how large the fluctuations are in comparison to the average number of infected individuals.

For very small γ, the model exhibits extremely high variability regardless of the coupling intensity D. This reflects the explosive outbreak regime, where abrupt transitions create strong dispersion in the time series. As γ increases, the variability drops rapidly. However, for intermediate and large values of γ, the system's behavior becomes strongly dependent on D.

For weaker couplings ($D = 10^{-5}$ and 10^{-4} day^{-1}), the CV reaches a local minimum around $\gamma \approx 5$ and then increases again, plateauing at larger values. This indicates that, under weak coupling, the increasing localization of the interaction is associated with greater temporal variability in the global infected population. In contrast, for intermediate and stronger couplings ($D \geq 10^{-3}$), the CV remains relatively low after the initial decrease and becomes only weakly dependent on γ, indicating a more uniform temporal evolution of the global epidemic activity.

Finally, to provide a global view of the epidemic dynamics, we now focus on global measures of the epidemic spread across the network. Fig. 10 shows colormaps of the average advancement rate v_m, the peak number of infected individuals $\mathcal{I}^{(peak)}$, and the extinction time τ, as a function of D and γ.

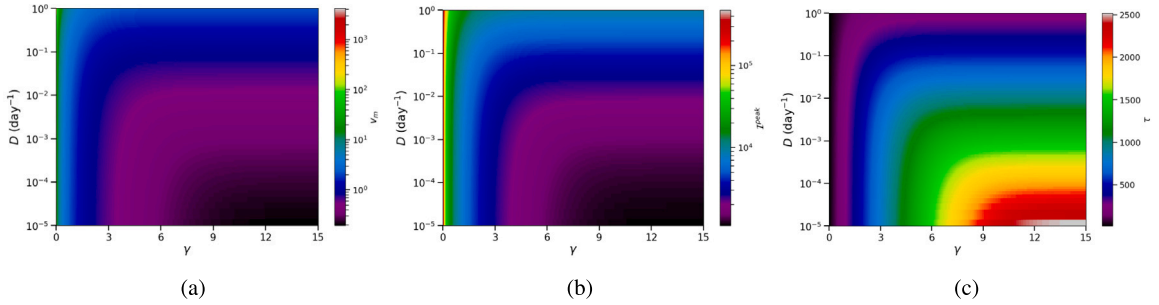


Fig. 10. Colormaps showing three global epidemic observables for the coupled SIR system as a function of the coupling intensity D (day^{-1}) and the interaction range γ: (a) average advancement rate v_m, (b) global infection peak $\mathcal{I}^{(peak)}$, and (c) extinction time τ. (For interpretation of the references to color in this figure legend, the reader is referred to the web version of this article.)

Fig. 10(a) shows the average advancement rate v_m across the parameter space. In the strong-coupling regime ($D \approx 1$ day^{-1}) combined with nearly global interactions ($\gamma \approx 0$), the system reaches maximum mean velocities of the order of 10^3 sites/day, as indicated by the bright region in the upper-left corner of the colormap. The interaction range plays a central role in this behavior since small values of γ correspond to long-range interactions that allow the infection to bypass spatial barriers and rapidly activate distant regions of the network. As γ increases and the interactions become progressively more localized, the epidemic spreads through spatially confined propagation fronts. In this regime, the mean velocity decreases substantially, particularly for weak coupling intensities D.

This change in the spreading dynamics is also reflected in the global infection peak $\mathcal{I}^{(peak)}$, presented in Fig. 10(b). For small values of γ, the long-range nature of the interactions promotes the almost simultaneous activation of distant regions, generating large outbreaks throughout the network. As a consequence, the $\mathcal{I}^{(peak)}$ reaches extremely high values that can exceed 10^5 infected individuals. In contrast, for larger γ, the localized character of the interactions spatially fragments the epidemic activity, preventing the entire network from reaching its maximum at the same time. The outbreaks therefore occur more heterogeneously across different regions, which significantly reduces the global infection peak.

The extinction time τ, shown in Fig. 10(c), follows a behavior strongly correlated with both the propagation velocity and the infection peak. In regimes characterized by long-range interactions and strong coupling, the outbreaks rapidly exhaust the susceptible population across the network, producing short epidemic lifetimes represented by the dark regions on the left side of the colormap. On the other hand, when the interactions are predominantly localized and the coupling intensity is weak, the epidemic activity remains spatially confined and persists for much longer times. The slower propagation delays the global depletion of susceptible individuals, leading to the large extinction times observed in the bright region located in the lower-right portion of the diagram.

While the epidemic dynamics are strongly controlled by the coupling intensity D and interaction range γ, an important question concerns whether the basic reproduction number R_0 [Eq. (4)], which summarizes the local epidemic potential, is sufficient to characterize the response of the spatially coupled system. Since R_0 depends on the epidemiological parameters β, α, and N_H, different combinations of these parameters can produce the exact same value of R_0. It is therefore essential to determine whether the epidemic dynamics depend primarily on R_0 or retain a significant dependence on the specific parameterization used to obtain it. For these analyses, the initial susceptible population is set to $S_j = N_H$ for all sites except the outbreak focus $j = 501$, where $S_{501} = N_H - 1$. Consequently, varying R_0 through N_H consistently scales the initial susceptible population with the reproduction number.

To address this question, we varied R_0 independently through the parameters β, α, and N_H, keeping the remaining parameters fixed in each case. Fig. 11 shows the resulting average advancement rate v_m and extinction time τ as functions of R_0 for different coupling configurations.

The numerical results reveal that the qualitative dependence of both observables on R_0 is remarkably robust to the specific parameter choice. In all coupling configurations, the average advancement rate v_m increases with R_0, whereas the extinction time τ decreases monotonically. This indicates that larger values of the basic reproduction number systematically favor faster spatial propagation and shorter epidemic lifetimes, independently of whether the change in R_0 is driven by β, α, or N_H. The persistence of these trends across different values of D and γ shows that this qualitative behavior is a fundamental feature of the spatially coupled system.

Although the overall qualitative trends are preserved, the different parameterizations of R_0 are not quantitatively equivalent. When R_0 is varied through β or N_H, the curves of both v_m and τ are nearly indistinguishable across the coupling configurations considered. In contrast, varying R_0 through the recovery rate α produces systematic deviations from these curves, particularly at larger values of R_0. For the present parameter range, the advancement rate obtained by varying α is larger than that obtained by varying β or N_H up to approximately $R_0 = 4.92$, after which the ordering is reversed. A similar crossover phenomenon is observed for the extinction time, showing that R_0 alone does not completely determine the quantitative spatial response.

When R_0 is increased through β or N_H, the average advancement rate v_m and extinction time τ exhibit nearly identical behavior, indicating that increasing the transmission rate or the initial susceptible population produces similar spatial epidemic dynamics. In

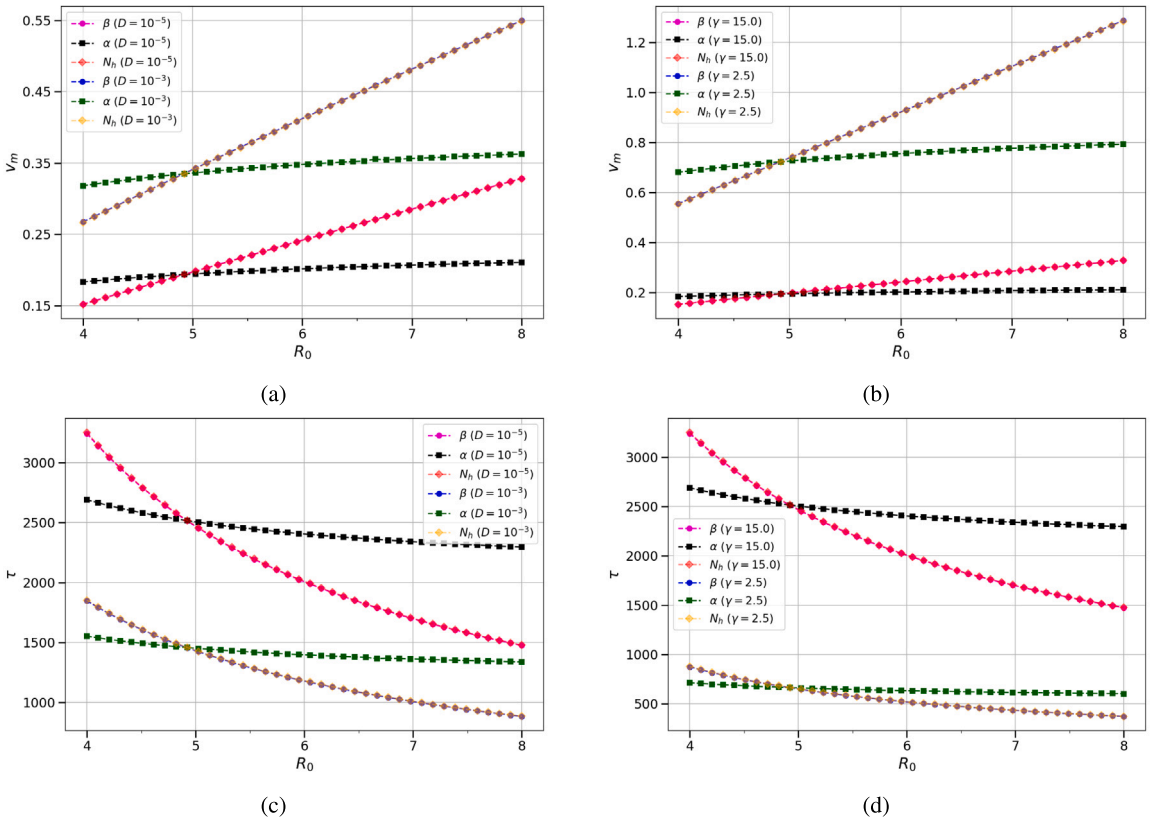


Fig. 11. Average advancement rate v_m (top row) and extinction time τ (bottom row) as functions of the basic reproduction number R_0. In all panels, R_0 is obtained by varying one of the parameters β, α, or N_H, while the remaining parameters are kept fixed. The left column shows results for different coupling intensities D with the coupling range fixed at $\gamma = 15$, while the right column corresponds to different coupling ranges γ with the coupling intensity fixed at $D = 10^{-5}$.

contrast, increasing R_0 by decreasing α has a comparatively weaker effect on both observables. Since $1/\alpha$ is associated with the mean residence time in the infected class (Ref. [15]), smaller α values prolong the infectious period and increase R_0; however, for $R_0 > 4.92$, this mechanism becomes less effective in promoting spatial propagation than increasing β or N_H. Thus, although these parameterizations can produce the same R_0, they are not quantitatively equivalent in determining the spatial dynamics of the epidemic.

These quantitative differences can be understood by considering how the recovery rate affects the temporal progression of the disease. In particular, increasing α accelerates the transition of infected individuals to the removed class, which modifies the temporal balance between transmission and recovery. This shift directly affects the number of susceptible individuals remaining after the epidemic, as illustrated in Fig. 12. Larger values of α lead to fewer cumulative infections and consequently to a larger remaining susceptible population across the network at the end of the outbreak. Therefore, although the same value of R_0 can be obtained through different parameter combinations, the resulting spatial epidemic trajectories need not be quantitatively identical.

The results further show that variations in the recovery rate α do not substantially alter the extinction time τ or the average advancement rate v_m compared with the differences observed for the other parameterizations of R_0. This suggests that, under the conditions considered here, variations in α have a comparatively limited effect on the total duration of the outbreak. However, this finding should be interpreted strictly within the assumptions of the present model, which omits disease-induced mortality and limitations in healthcare capacity. Incorporating such real-world features would likely amplify the distinct dynamical role played by the recovery parameter.

In summary, the spreading dynamics of the coupled SIR model are governed by an interplay between the coupling intensity D and the interaction range γ. In the global coupling limit ($\gamma = 0$), the epidemic exhibits rapid spatial spreading accompanied by extreme infection peaks. For intermediate values of γ, corresponding to long-range interactions, the spreading dynamics progressively develop spatial structure while still allowing efficient transport across distant regions of the lattice. In the nearest-neighbor coupling limit, the epidemic becomes constrained to a traveling-wave regime characterized by a well-defined effective propagation velocity.

Furthermore, the onset of the strong-coupling regime systematically reshapes the spatial profile of the propagation front, leading to enhanced spreading velocities near the outbreak focus. Together, these results demonstrate that the spatial reach and intensity of

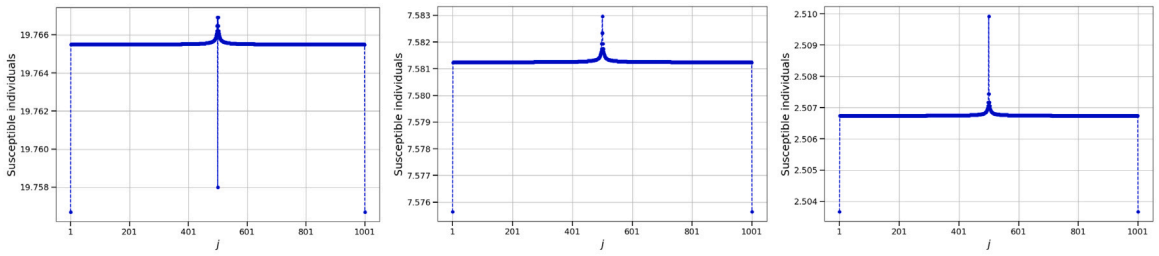


Fig. 12. Number of susceptible individuals at each site at the final simulation time for (a) $\alpha = 0.585$ with $R_0 = 4.00$, (b) $\alpha = 0.476$ with $R_0 = 4.92$, and (c) $\alpha = 0.390$ with $R_0 = 6.00$. We consider $N_H = 1000$, $\beta = 0.002342, \text{day}^{-1}$, $\gamma = 15$, and $D = 10^{-5}, \text{day}^{-1}$.

the interactions fundamentally control not only the propagation velocity of the disease, but also the global dynamical organization of the epidemic, highlighting the central role of spatial coupling structures in epidemic spread and containment.

4. Conclusion

In this work, we investigated the spatiotemporal dynamics of epidemic propagation in a chemically coupled SIR model, focusing on how the coupling intensity D and the interaction range γ shape the spreading behavior across the network. Our results reveal the existence of distinct propagation regimes controlled by the spatial structure of the interactions. In the global coupling limit ($\gamma = 0$), the epidemic spreads rapidly throughout the lattice, producing large outbreak peaks and highly accelerated propagation fronts. As the interaction range becomes more localized, the dynamics progressively transition toward traveling-wave-like propagation with finite front velocities.

A central result of this work is the emergence of a strong-coupling regime characterized by a nonmonotonic spatial profile of the advancement rates, in which the epidemic front becomes significantly accelerated near the outbreak site. To quantify the onset of this regime, we introduced the critical coupling parameter D_{crit} and showed that its dependence on γ follows an exponential crossover law of the form $D_{crit}(\gamma) \sim ce^{-a\gamma} + D_{\text{plateau}}$. This scaling behavior indicates a smooth transition between global, long-range, and nearest-neighbor interaction regimes, establishing a direct connection between the spatial reach of the coupling and the dynamical organization of the epidemic front.

The global observables further demonstrate that the interaction range controls not only the propagation velocity, but also the temporal stability and variability of the epidemic dynamics. In particular, long-range interactions favor explosive outbreaks with large fluctuations, whereas localized interactions lead to smoother propagation fronts and more structured temporal dynamics. These results highlight the fundamental role of spatial coupling mechanisms in epidemic spread and suggest that modifying the effective interaction range may strongly affect both outbreak intensity and propagation efficiency.

The main contribution of this work is the identification and characterization of the nonmonotonic strong-coupling propagation regime and the associated critical threshold $D_{crit}(\gamma)$. The chemical-coupling formulation provides the nonlocal, diffusion-mediated spatial interaction through which this behavior emerges. This regime, in which the epidemic front becomes locally accelerated near the outbreak focus rather than uniformly faster throughout the network, demonstrates that the spatial coupling mechanism can alter not only the propagation speed but also the qualitative organization of epidemic spreading.

The present analysis was carried out on a one-dimensional ring network, which allowed a controlled, fully parameterized exploration of the coupling intensity D and interaction range γ but does not correspond to any specific real-world geography. Extending this framework to two-dimensional or graph-structured topologies, better suited to representing real metapopulation networks, remains an important direction for future work.

As future work, we also propose extending the framework by considering alternative epidemiological models, including formulations that incorporate additional compartments such as vaccinated individuals and vector-mediated transmission. Such extensions may provide a more realistic description of disease dynamics while preserving the same underlying interaction structure. In particular, exploring how different epidemiological mechanisms interact with spatial coupling may reveal nontrivial effects on outbreak propagation and variability. Additionally, stochastic fluctuations and individual-based descriptions could be incorporated to better capture the role of randomness in both transmission and demographic processes. Finally, intervention strategies such as vaccination policies and control measures could be systematically investigated within this framework to assess their impact across different epidemiological regimes.

CRediT authorship contribution statement

Vitor H.A. Fávaro: Writing – review & editing, Writing – original draft, Visualization, Validation, Software, Methodology, Investigation, Formal analysis, Data curation. **Ricardo L. Viana:** Writing – review & editing, Validation, Methodology, Formal analysis. **João P.V. Ramalho:** Software, Methodology, Formal analysis. **Jane Rosa:** Writing – review & editing, Validation, Supervision, Software, Resources, Project administration, Methodology, Investigation, Funding acquisition, Formal analysis, Conceptualization.

Declaration of competing interest

The authors declare that they have no known competing financial interests or personal relationships that could have appeared to influence the work reported in this paper.

Acknowledgments

The authors acknowledge financial support from the Coordenação de Aperfeiçoamento de Pessoal de Nível Superior (CAPES, Grant Nos. 88887.954987/2024-00 and 88881.143103/2017-01) and the Conselho Nacional de Desenvolvimento Científico e Tecnológico (CNPq, Grant Nos. 403120/2021-7 and 301019/2019-3). Vitor Hugo Alexandrino Fávaro and Jane Rosa are grateful to Prof. Dr. Fábio Alliguieri dos Santos Silva for valuable discussions on chemical coupling and for his support in the development of the first version of the network numerical code. The authors also acknowledge the Programa Institucional de Bolsas de Iniciação Científica of the Instituto Federal do Paraná (PIBIC/IFPR). In addition, Vitor Hugo Alexandrino Fávaro acknowledges the Fundação Araucária de Apoio ao Desenvolvimento Científico e Tecnológico do Estado do Paraná (Fundação Araucária) and CNPq for an undergraduate research scholarship.

Data availability

Data will be made available on request.

References

[1] Anderson RM, May RM. Infectious diseases of humans: Dynamics and control. Oxford University Press; 1991.
[2] Murray JD. Mathematical biology. I: An introduction. third ed.. Springer; 2002.
[3] Keeling MJ, Rohani P. Modeling infectious diseases in humans and animals. Princeton University Press; 2008.
[4] Viboud C, Bjørnstad ON, Smith DL, Simonsen L, Miller MA, Grenfell BT. Synchrony, waves, and spatial hierarchies in the spread of influenza. Science 2006;312(5772):447–51. http://dx.doi.org/10.1126/science.1125237.
[5] Joh RI, Wang H, Weiss H, Weitz JS. Dynamics of indirectly transmitted infectious diseases with immunological threshold. Bull Math Biol 2009;71(4):845–62. http://dx.doi.org/10.1007/s11538-008-9384-4.
[6] Perofsky AC, Hansen CL, Burstein R, Boyle S, Prentice R, Marshall C, Reinhart D, Capodanno B, Truong M, Schwabe-Fry K, Kuchta K, Pfau B, Acker Z, Lee J, Sibley TR, McDermot E, Rodriguez-Salas L, Stone J, Gamboa L, Han PD, Adler A, Waghmare A, Jackson ML, Famulare M, Shendure J, Bedford T, Chu HY, Englund JA, Starita LM, Viboud C. Impacts of human mobility on the citywide transmission dynamics of 18 respiratory viruses in pre- and post-COVID-19 pandemic years. Nat Commun 2024;15(4164). http://dx.doi.org/10.1038/s41467-024-48528-2.
[7] Lessani MN, Li Z, Jing F, Qiao S, Zhang J, Olatosi B, Li X. Human mobility and the infectious disease transmission: A systematic review. Geo-Spat. Inf Sci 2024;27(6):1824–51. http://dx.doi.org/10.1080/10095020.2023.2275619.
[8] Colizza V, Barrat A, Barthélemy M, Vespignani A. The role of the airline transportation network in the prediction and predictability of global epidemics. Proc Natl Acad Sci USA 2006;103(7):2015–20. http://dx.doi.org/10.1073/pnas.0510525103.
[9] Balcan D, Colizza V, Gonçalves B, Hu H, Ramasco JJ, Vespignani A. Multiscale mobility networks and the spatial spreading of infectious diseases. Proc Natl Acad Sci USA 2009;106(51):21484–9. http://dx.doi.org/10.1073/pnas.0906910106.
[10] Stoddard ST, Morrison AC, Vazquez-Prokopec GM, Soldan VP, Kochel TJ, Kitron U, Elder JP, Scott TW. The role of human movement in the transmission of vector-borne pathogens. PLoS Negl Trop Dis 2009;3(7):e481. http://dx.doi.org/10.1371/journal.pntd.0000481.
[11] Riley S. Large-scale spatial-transmission models of infectious diseases. Science 2007;316(5829):1298–301. http://dx.doi.org/10.1126/science.1134695.
[12] Arino J, van den Driessche P. A multi-city epidemic model. Math Popul Stud 2003;10(3):175–93. http://dx.doi.org/10.1080/08898480306720.
[13] Sattenspiel L, Dietz K. A structured epidemic model incorporating geographic mobility among regions. Math Biosci 1995;128(1–2):71–91. http://dx.doi.org/10.1016/0025-5564(94)00068-B.
[14] Chinazzi M, Davis JT, Ajelli M, Gioannini C, Litvinova M, Merler S, Pastore y Piontti A, Mu K, Rossi L, Sun K, Viboud C, Xiong X, Yu H, Halloran ME, Longini Jr. IM, Vespignani A. The effect of travel restrictions on the spread of the 2019 novel coronavirus (COVID-19). Science 2020;368(6489):395–400. http://dx.doi.org/10.1126/science.aba9757.
[15] Martcheva M. An introduction to mathematical epidemiology. 1st ed.. Gainesville: Springer; 2015.
[16] Hethcote HW. The mathematics of infectious diseases. SIAM Rev 2000;42(4):599–653. http://dx.doi.org/10.1137/S0036144500371907.
[17] Diekmann O, Heesterbeek JAP. Mathematical epidemiology of infectious diseases: Model building, analysis and interpretation. First. Wiley; 2000.
[18] Schaber KL, Perkins TA, Lloyd AL, Waller LA, Kitron U, Paz-Soldan VA, Elder JP, Rothman AL, Civitello DJ, Elson WH, Morrison AC, Scott TW, Vazquez-Prokopec GM. Disease-driven reduction in human mobility influences human–mosquito contacts and dengue transmission dynamics. PLoS Comput Biol 2021;17(1):e1008627. http://dx.doi.org/10.1371/journal.pcbi.1008627.
[19] Gubler DJ. Dengue and dengue hemorrhagic fever. Clin Microbiol Rev 1998;11(3):480–96. http://dx.doi.org/10.1128/CMR.11.3.480.
[20] Stoddard ST, Forshey BM, Morrison AC, Paz-Soldan VA, Vazquez-Prokopec GM, Astete H, Reiner RC, Vilcarromero S, Elder JP, Halsey ES, Kochel TJ, Kitron U, Scott TW. House-to-house human movement drives dengue virus transmission. Proc Natl Acad Sci USA 2013;110(3):994–9. http://dx.doi.org/10.1073/pnas.1213349110.
[21] Faria NR, Kraemer MUG, Hill SC, Goes de Jesus J, Aguiar RS, Iani FCM, Xavier J, Quick J, du Plessis L, Dellicour S, Thézé J, Carvalho RDO, Baele G, Wu C-H, Silveira PP, Arruda MB, Pereira MA, Pereira GC, Lourenço J, Obolski U, Abade L, Vasylyeva TI, Giovanetti M, Yi D, Weiss DJ, Wint GRW, Shearer FM, Funk S, Nikolay B, Fonseca V, Adelino TER, Oliveira MAA, Silva MVF, Sacchetto L, Figueiredo PO, Rezende IM, Mello E, Said RFC, Santos DA, Ferraz ML, Brito MG, Santana LF, Menezes MT, Brindeiro RM, Tanuri A, Dos Santos FCP, Cunha MS, Nogueira JS, Rocco IM, da Costa AC, Komninakis SCV, Azevedo V, Chieppe AO, Araujo ESM, Mendonça MCL, Dos Santos CC, Dos Santos CD, Mares-Guia AM, Nogueira RMR, Sequeira PC, Abreu RG, Garcia MHO, Abreu AL, Okumoto O, Kroon EG, de Albuquerque CFC, Lewandowski K, Pullan ST, Carroll M, de Oliveira T, Sabino EC, Souza RP, Suchard MA, Lemey P, Trindade GS, Drumond BP, Filippis AMB, Loman NJ, Cauchemez S, Alcantara LCJ, Pybus OG. Genomic and epidemiological monitoring of yellow fever virus transmission. Science 2017;361(6405):894–9. http://dx.doi.org/10.1126/science.aat7115.
[22] Cavany SM, España G, Vázquez-Prokopec GM, Scott TW, Perkins TA. Pandemic-associated mobility restrictions could cause increases in dengue virus transmission. PLoS Negl Trop Dis 2021;15(8):e0009603. http://dx.doi.org/10.1371/journal.pntd.0009603.

[23] Bomfim R, Pei S, Shaman J, Yamana T, Makse HA, Andrade Jr JS, Furtado V. Predicting dengue outbreaks at neighbourhood level using human mobility in urban areas. J R. Soc Interface 2020;17(171):20200691. http://dx.doi.org/10.1098/rsif.2020.0691.

[24] Ospina-Aguirre C, Soriano-Paños D, Olivar-Tost G, Galindo-González CC, Gómez-Gardeñes J, Osorio G. Effects of human mobility on the spread of dengue in the region of caldas, Colombia. PLoS Negl Trop Dis 2023;17(11):e0011087. http://dx.doi.org/10.1371/journal.pntd.0011087.

[25] Keeling MJ, Eames KTD. Networks and epidemic models. J R. Soc Interface 2005;2(4):295–307. http://dx.doi.org/10.1098/rsif.2005.0051.

[26] Ruan S, Wang W. Dynamical behavior of an epidemic model with a nonlinear incidence rate. J Differential Equations 2003;188(1):135–63. http://dx.doi.org/10.1016/S0022-0396(02)00089-6.

[27] Kermack WO, Mckendrick AG. A contribution to the mathematical theory of epidemics. Proc R. Soc Lond Ser A 1927;155:700–21.

[28] Lloyd AL, May RM. Spatial heterogeneity in epidemic models. J Theoret Biol 1996;179(1):1–11. http://dx.doi.org/10.1006/jtbi.1996.0042.

[29] Pastor-Satorras R, Vespignani A. Epidemic spreading in scale-free networks. Phys Rev Lett 2001;86(14):3200. http://dx.doi.org/10.1103/PhysRevLett.86.3200.

[30] Newman MEJ. Spread of epidemic disease on networks. Phys Rev E 2002;66(1):016128. http://dx.doi.org/10.1103/PhysRevE.66.016128.

[31] Grenfell BT, Bjørnstad ON, Kappey J. Travelling waves and spatial hierarchies in measles epidemics. Nature 2001;414(6865):716–23. http://dx.doi.org/10.1038/414716a.

[32] Kissler SM, Tedijanto C, Goldstein E, Grad YH, Lipsitch M. Projecting the transmission dynamics of SARS-CoV-2 through the postpandemic period. Science 2020;368(6493):860–8. http://dx.doi.org/10.1126/science.abb5793.

[33] Cosner C, Beier JC, Cantrell RS, Impoinvill D, Kapitanski L, Potts MD, Troyo A, Ruan S. The effects of human movement on the persistence of vector-borne diseases. J Theoret Biol 2009;258(4):550–60. http://dx.doi.org/10.1016/j.jtbi.2009.02.016.

[34] Fávaro VHA, Gabrick EC, Batista AM, Caldas IL, Viana RL. Epidemiological model based on networks with non-local coupling. Chaos Solitons Fractals 2023;177:114256. http://dx.doi.org/10.1016/j.chaos.2023.114256.

[35] Zhu L, Zheng T. Pattern dynamics analysis and application of west nile virus spatiotemporal models based on higher-order network topology. Bull Math Biol 2025;87:121. http://dx.doi.org/10.1007/s11538-025-01501-6.

[36] Dai S, Zhu L, He L, Dong Y. Dynamics and control of infectious diseases on complex networks: A theoretical and empirical study. J Math Anal Appl 2026;557:130334. http://dx.doi.org/10.1016/j.jmaa.2025.130334.

[37] Brockmann D, Helbing D. The hidden geometry of complex, network-driven contagion phenomena. Science 2013;342(6164):1337–42. http://dx.doi.org/10.1126/science.1245200.

[38] Hanski I. Metapopulation dynamics. Nature 1998;396:41–9. http://dx.doi.org/10.1038/23876.

[39] Watts DJ, Muhamad R, Medina DC, Dodds PS. Multiscale, resurgent epidemics in a hierarchical metapopulation model. Proc Natl Acad Sci USA 2005;102(32):11157–62. http://dx.doi.org/10.1073/pnas.0501226102.

[40] Xia Y, Bjørnstad ON, Grenfell BT. Measles metapopulation dynamics: a gravity model for epidemiological coupling and dynamics. Amer Nat 2004;164(2):267–81. http://dx.doi.org/10.1086/422341.

[41] Hufnagel L, Brockmann D, Geisel T. Forecast and control of epidemics in a globalized world. Proc Natl Acad Sci USA 2004;101(42):15124–9. http://dx.doi.org/10.1073/pnas.0308344101.

[42] Bichara D, Iggidr A. Multi-patch and multi-group epidemic models: A new framework. J Math Biol 2018;77:107–34. http://dx.doi.org/10.1007/s00285-017-1191-9.

[43] Kabir KMA, Tanimoto J. Impact of awareness in metapopulation epidemic model to suppress the infected individuals for different graphs. Eur Phys J B 2019;92(9):199. http://dx.doi.org/10.1140/epjb/e2019-90570-7.

[44] Barrat A, Barthélemy M, Vespignani A. Dynamical processes on complex networks. Cambridge University Press; 2008.

[45] Pastor-Satorras R, Castellano C, Van Mieghem P, Vespignani A. Epidemic processes in complex networks. Rev Modern Phys 2015;87(3):925–79. http://dx.doi.org/10.1103/RevModPhys.87.925.

[46] Mollison D. Spatial contact models for ecological and epidemic spread. J R. Stat Soc Ser B 1977;39(3):283–326. http://dx.doi.org/10.1111/j.2517-6161.1977.tb01627.x.

[47] Diekmann O. Thresholds and travelling waves for the geographical spread of infection. J Math Biol 1978;6(2):109–30. http://dx.doi.org/10.1007/BF02450783.

[48] Medlock J, Kot M. Spreading disease: integro-differential equations old and new. Math Biosci 2003;184(2):201–22. http://dx.doi.org/10.1016/S0025-5564(03)00041-5.

[49] Colizza V, Pastor-Satorras R, Vespignani A. Reaction–diffusion processes and metapopulation models in heterogeneous networks. Nat Phys 2007;3(4):276–82. http://dx.doi.org/10.1038/nphys560.

[50] Colizza V, Vespignani A. Epidemic modeling in metapopulation systems with heterogeneous coupling pattern: Theory and simulations. J Theoret Biol 2008;251(3):450–67. http://dx.doi.org/10.1016/j.jtbi.2007.11.028.

[51] Filipe JAN, Maule MM. Effects of dispersal mechanisms on spatio-temporal development of epidemics. J Theoret Biol 2004;226(2):125–41. http://dx.doi.org/10.1016/j.jtbi.2003.08.014.

[52] Keeling MJ. The effects of local spatial structure on epidemiological invasions. Proc R. Soc Lond B 1999;266(1421):859–67. http://dx.doi.org/10.1098/rspb.1999.0716.

[53] Shi J, Zhu L. Turing pattern theory on homogeneous and heterogeneous higher-order temporal network system. J Math Phys 2025;66:042706. http://dx.doi.org/10.1063/5.0211728.

[54] Viana RL, Batista AM, Batista CAS, de Pontes JCA, Silva FAS, Lopes SR. Bursting synchronization in networks with long-range coupling mediated by a diffusing chemical substance. Commun Nonlinear Sci Numer Simul 2012;17(7):2924–42. http://dx.doi.org/10.1016/j.cnsns.2011.11.016.

[55] Silva FAS, Lopes SR, Viana RL. Synchronization of biological clock cells with a coupling mediated by the local concentration of a diffusing substance. Commun Nonlinear Sci Numer Simul 2016;35:37–52. http://dx.doi.org/10.1016/j.cnsns.2015.11.003.

[56] Czajkowski BM, Batista CAS, Viana RL. Synchronization of phase oscillators with chemical coupling: Removal of oscillators and external feedback control. Phys A 2023;610:128418. http://dx.doi.org/10.1016/j.physa.2022.128418.

[57] Haerter P, Viana RL. Synchronization of phase oscillators due to nonlocal coupling mediated by the slow diffusion of a substance. Braz J Phys 2023;53(114). http://dx.doi.org/10.1007/s13538-023-01327-4.

[58] Kuramoto Y. Chemical oscillations, waves, and turbulence. Springer; 1984.

[59] Kuramoto Y. Scaling behavior of turbulent oscillators with non-local interaction. Progr Theoret Phys 1995;94(3):321–30. http://dx.doi.org/10.1143/PTP.94.321.

[60] Kuramoto Y, Nakao H. Power-law spatial correlations and the onset of individual motions in self-oscillatory media with non-local coupling. Phys D 1997;103(1):294–313. http://dx.doi.org/10.1016/S0167-2789(96)00264-3.

[61] Kuramoto Y, Nakao H. Origin of power-law spatial correlations in distributed oscillators and maps with nonlocal coupling. Phys Rev Lett 1996;76(23):4352–5. http://dx.doi.org/10.1103/PhysRevLett.76.4352.

[62] Arenas A, Díaz-Guilera A, Kurths J, Moreno Y, Zhou C. Synchronization in complex networks. Phys Rep 2008;469:93–153. http://dx.doi.org/10.1016/j.physrep.2008.09.002.

[63] Kazanci GF, Ermentrout B. Pattern formation in an array of oscillators with electrical and chemical coupling. SIAM J Appl Math 2007;67(2):512–29. http://dx.doi.org/10.1137/060661041.